

# Experimental observations of the mixing transition in a shock-accelerated gas curtain

P. M. Rightley, P. Vorobieff, R. Martin,<sup>a)</sup> and R. F. Benjamin  
*Los Alamos National Laboratory, Los Alamos, New Mexico 87545*

(Received 6 March 1998; accepted 22 September 1998)

Richtmyer–Meshkov instability of a thin curtain of heavy gas ( $\text{SF}_6$ ) embedded in air and accelerated by a planar shock wave (Mach 1.2) leads to the growth of interfacial perturbations in the curtain and to mixing. Our experiments produce a phenomenological description of the mixing transition and incipient turbulence during the first millisecond after the shock interaction. Growth of scales both larger and smaller than that of initial perturbations is visually observed and quantified by applying a wavelet transform to laser-sheet images of the evolving gas curtain. Histogram and wavelet analyses show an abrupt mixing transition for a multimode initial perturbation that is not apparent for single-mode perturbations. [S1070-6631(99)00501-2]

## I. INTRODUCTION

The Richtmyer–Meshkov (RM) instability results from impulsive acceleration of density interfaces. Both RM and its constant-acceleration analog, Rayleigh–Taylor (RT) instability, result from the acceleration of inhomogeneities in the flow (i.e., density gradients) and are vortex driven via baroclinic generation of torque. Likewise, both produce flow patterns of bubbles and spikes. Unlike RT, RM causes density interfaces to become unstable regardless of orientation (i.e., acceleration going from heavy to light fluid or vice versa). Although linear analysis of both instabilities produces significantly different growth rates (linear growth for RM and exponential growth for RT), both lead to rapid distortion of the interface, to mixing, and eventually to turbulence. Our analysis of the mixing phase of the RM instability provides quantitative measures of the transition from deterministic instability growth to mixing and incipient turbulence. We seek a phenomenological description of this mixing, apparently caused by strain in the flow field and the interaction of flow structures, such as bubbles, spikes, and vortex pairs—characteristic features of fluid interpenetration.

Applications of RM- and RT-induced mixing range from the microscopic to the cosmological. In inertial confinement fusion, the RM and RT instabilities have hampered the ability to produce useful energy by limiting the final compression and mixing the ablative capsule material with the interior fuel.<sup>1</sup> The RM instability has been used to explain the unexpected lack of significant stratification of the products of supernova 1987A.<sup>2,3</sup> In these applications, the concern is not with the early time behavior of the instability flow (which has been investigated experimentally, theoretically, and numerically), but with the consequent late-time mixing and eventual turbulence.

The earliest experimental studies of the RM instability looked at a single interface between gases of different densities. The interface was produced by separating the gases

with a thin membrane<sup>4,5</sup> and interrogating the flow with shadowgraphy or schlieren. In these studies, membrane fragments influence the development of the flow, especially the small scales at late times. Also, the line-of-sight integration of the diagnostics (schlieren, shadowgraphy, or radiography) eliminates much of the information from the smallest spatial scales. Benjamin and Fritz<sup>6</sup> performed a similar test using high explosively driven liquids. Again, the diagnostics failed to record the information of the small scales. Also, the arrival of the Taylor wave from the HE driver complicated the interpretation of the late-time images by also inducing the RT instability.

Brouillette and Sturtevant<sup>7,8</sup> were the first to produce shock-accelerated diffuse gaseous interfaces without membranes. They set initial conditions by stratification in a vertical shock tube experiment, but their diagnostic was still line-of-sight integration. Several other experiments<sup>9–11</sup> have generated membrane-less diffuse interfaces in vertical shock tubes. Later Jacobs *et al.*<sup>12</sup> and Budzinski *et al.*<sup>13</sup> developed a more precise diagnostic technique by illuminating diffuse-interface flow in a horizontal shock tube with a laser sheet. These laser-sheet studies, like ours, use a thin layer of gas (a “gas curtain”) embedded within the ambient air. Consequently, RM instability occurs at two nearby interfaces. Larger initial amplitude perturbations on the upstream interface relative to those on the downstream and vice versa, i.e., streamwise-asymmetric initial conditions, develop into asymmetric flow evolution patterns. More vorticity is produced on the interface with larger perturbations, thereby causing instability growth to be more prominent at that interface.

Instability growth rates could not be accurately determined in the early light-sheet experiments<sup>12,13</sup> because only one or two images per event could be captured. The diffuse interfaces stabilized the smaller wavelengths at early time, and the limited temporal resolution prevented the investigation of late-time transition to turbulence and mixing. Recent horizontal shock-tube studies<sup>14</sup> have overcome the temporal resolution limitations. In these experiments, as well as in the

<sup>a)</sup>Current address: University of California, Santa Barbara, CA 93106.

experiments presented here, the Reynolds number for the initial stage of the flow evolution based on the perturbation wavelength (6 mm), characteristic perturbation velocity (10 m/s), and the kinematic viscosity of SF<sub>6</sub> is  $R = 2 \times 10^4$ , indicating a strong tendency toward turbulence.

The nature of the mixing transition resulting from the RM instability and subsequent turbulence has been difficult to characterize because of experimental limitations (membrane effects, spatial/temporal resolution) until recently. Studies have shown that the Kelvin–Helmholtz (KH) instability of free shear layers progresses through complex, predictable steps prior to the transition to turbulence. Streamwise vorticity superimposed on the dominant spanwise vortex structures begins a cascade of energy to smaller scales,<sup>15–18</sup> while the coalescence of the spanwise structures produces larger scales. After the three-dimensional vorticity field has developed for some time, the flow breaks down (at the “mixing transition”) into a highly disordered state.

Presently, there exists no developed theory describing all the steps of the RM instability and the consequent transition to turbulence. Visual analysis of gas-curtain experiments shows three stages in the flow evolution toward turbulence. Immediately following the shock-wave acceleration, RM instability causes a vortex-dominated flow<sup>19</sup> in which the prominent coherent structures are pairs of counterrotating vortices manifest as “mushroom caps” in laser sheet images. The first stage is deterministic and can be accurately predicted with adaptive-grid simulations<sup>20</sup> or qualitatively reproduced with a simple vortex-blob model.<sup>14</sup> The second stage is characterized by the coexistence of deterministic (large scale) and disordered (small scale) flow as strain increases and interaction between vortex pairs becomes relevant.<sup>21</sup> This interaction (mode coupling) and emergence of small-scale three dimensionality are important during the third stage which is largely disordered. Numerical simulations predict the behavior of the deterministic part of the flow reasonably well, but cannot reliably describe the behavior of the disordered component, which is crucial to mixing. Here it is worthwhile to note a difference between the investigations of RM instability and the classic studies of free shear layers. Many of the latter are unforced (no external perturbation). In our RM experiments, the initial perturbations are imposed upon the interface prior to shock acceleration. Thus in some sense RM would be analogous to forced shear layer experiments. In our setting, the case similar to unforced shear layer would be that of a gas curtain with initially flat interfaces, which is not investigated here.

Our analysis of the experimental data concentrates primarily on a quantitative phenomenological description of the mixing transition in a shock-accelerated gas curtain. What analysis methods are suitable for the purpose?

We consider several techniques, including histogram analysis, wavelet, and Fourier transform. The specific features of the gas curtain flow that we regard as crucial for the right choice of analysis procedures are transience, inhomogeneity, the presence of strong density gradients, and the importance of coherent features.

A density (proportional to scattered light intensity) histogram analysis determining the frequency of appearance of

density values is particularly appropriate in locating a mixing transition in a flow initially characterized by density gradients. As the two species mix, producing densities intermediate to either “pure” species, the histograms evolve in time. An abrupt decrease in the histogram for densities of one or the other of the species is indicative of the mixing transition.

Application of wavelets to the study of transitional processes is new, although wavelet transform has been successfully employed in numerous studies of developed turbulence. Because this integral transform uses a basis of spatially localized functions, it is particularly useful for identification and quantification of coherent structures. In our case, such coherent structures are the vortices that dominate the flow in the interval between the early instability growth and the onset of turbulence. These structures should produce a signature clearly identifiable in the wavelet transform space, which contains both the scale and physical space information. This makes it possible to quantify the characteristic locations and sizes of coherent structures. The reviews by Farge<sup>22</sup> and by Farge *et al.*<sup>23</sup> describe the wavelet techniques that can be employed in studies of turbulence and refer to numerous such studies. Most of these studies deal with numerical simulations. Among the noteworthy experimental works, we will mention two. Everson *et al.*<sup>24</sup> used wavelets in their study of three-dimensional jet turbulence to analyze images of passive scalar (dye) advected by the flow. Voro-bieff and Rockwell<sup>25</sup> employed wavelet transforms to recover information about the scale and location of a particular coherent structure in the vorticity field acquired in turbulent stalling flow under a maneuvering delta wing. The latter study is of particular interest because it applied the idea of topological flow decomposition via wavelets to experimental data. This idea utilizes the knowledge about the flow to construct the wavelet basis in such a way that in the transform plane coherent structures specific to the flow have an easily identifiable signature. For the present study, the erosion of this signature would indicate transition to a disordered state.

Methods based on Fourier transform, although employed in many turbulence studies, are not utilized in this work. The strength of these methods lies in the possibility of comparison of experimental data with theoretical results. However, most of the theories apply only to fully developed, homogeneous, uniform-density turbulence. Our flow, as well as other instability flows, e.g., Kelvin–Helmholtz or Rayleigh–Taylor, is driven by density gradients and is spatially inhomogeneous and time dependent. To date, there is no well-developed statistical theory for such flows. The excellent 1974 work of Kraichnan<sup>26</sup> provides analysis of the theoretical ideas about the statistics of the inertial range in turbulent flows. This work could be a good starting point for someone attempting to create a statistical theory of inhomogeneous turbulence.

The important role the interaction of coherent structures plays during the mixing transition also raises concern about the applicability of the Fourier techniques. In particular, Fourier spectral methods are problematic for providing a phenomenological description of our flow. It would be desirable to quantify the properties of the coherent structures, and Fourier transform spreads the information about each individual

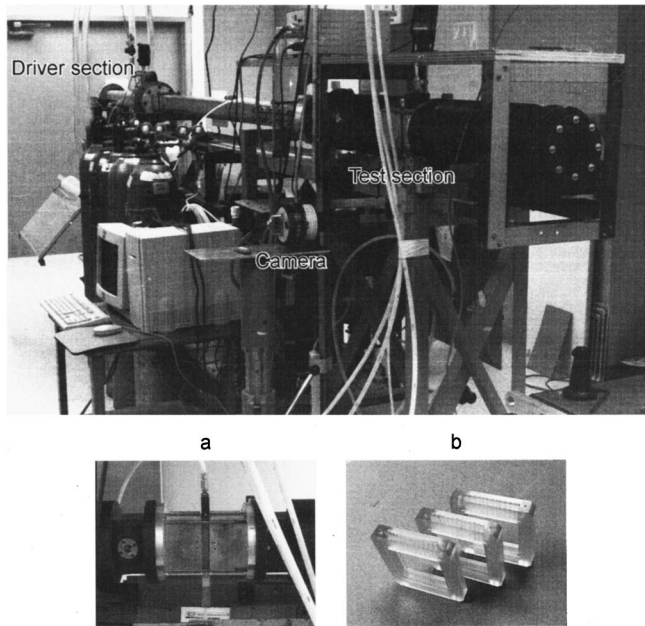


FIG. 1. View of the DX-3 gas shock tube: (a) test section, (b) injection nozzles.

structure (e.g., vortex) across the transform space, with spatial features manifesting themselves primarily in the phase plane, not the amplitude plane. Thus, as Armi and Flament show,<sup>27</sup> this information is lost in the process of obtaining the power spectrum, and the shapes of amplitude spectra are weakly related with the spatial structure of the flow. Consequently, we use histograms and wavelet transforms for our phenomenological analysis in order to focus on the mixing transition. Besides helping one to understand the physics of the mixing transition, our quantitative results can be utilized for code benchmarking.

Section II discusses the experiment and diagnostics including the several methods of improving spatial and temporal resolution of images from the shock-driven events. Section III qualitatively describes the flow morphologies resulting from both single-mode and multimode initial conditions. Quantitative analysis of the images aimed at understanding the evolution of the instability flow are presented in Sec. IV. Along with the application of wavelet transforms to the images, a density histogram analysis shows the existence of a mixing transition occurring within the flow.

## II. EXPERIMENTAL DETAILS

### A. Experimental facility

The 5.5 m shock tube employed in the experiments is shown in Fig. 1. The cross section of the tube is square with a side of 75 mm. The driver section, pressurized to 140 kPa gauge pressure before the shot, is separated from the rest of the tube at ambient pressure by a polypropylene diaphragm. A solenoid-actuated scalpel ruptures the diaphragm, producing a Mach 1.2 planar shock wave propagating in the air of the driven section. There is a temporal uncertainty inherent in the creation of the shock, so the test section diagnostics are triggered by the passage of the shock wave past three

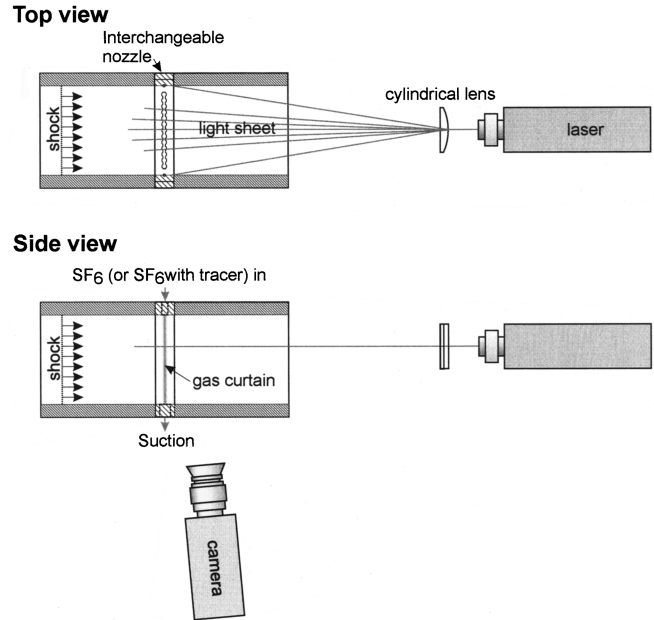


FIG. 2. Schematic of the test section, optical diagnostics, and curtain generation.

piezoelectric pressure transducers flush mounted on the wall of the driven section. The first two transducers are employed to measure the velocity and pressure jump of the shock. The third transducer, adjacent to the test section, triggers the optical diagnostics.

A vertical “curtain” of  $\text{SF}_6$  (pure or mixed with tracers) is injected through a nozzle in the top of the test section and removed through an exhaust plenum in the test section bottom [Figs. 1(a) and 2]. Both the injection nozzle and the exhaust plenum are flush with the test section wall. The contour of the injection nozzle imposes a perturbation on the cross section of the curtain. Interchangeable nozzles [Figs. 1(b) and 3] make it possible to create initial conditions containing one or more perturbation wavelengths. The velocity in the curtain is on the order of 10 cm/s. The direction of the  $\text{SF}_6$  flow (downward) improves the curtain stability and two dimensionality. To further reduce shear instability at the  $\text{SF}_6$ /air interfaces and reduce the contamination of surrounding air masses by  $\text{SF}_6$ , the volumetric flow rate through the exhaust plenum is chosen to be greater than that through the injection nozzle, so that some of the ambient air adjacent to the curtain is also removed from the test section. To provide replenishment for the air, two open ports (far upstream and far downstream of the curtain) connect the interior of the shock tube with the ambient atmosphere. Variation of the curtain velocity within the range 5–10 cm/s from experiment to experiment does not produce an observable influence on the initial conditions. Visual checks confirm that the flow in the curtain is laminar.<sup>14</sup> The curtain flow takes 5–10 s to stabilize after the initialization. The scalpel rupturing the diaphragm is actuated immediately after the flow becomes steady. Small changes in this flow over time lead to initial conditions varying from shot to shot for each nozzle. Although the initial conditions are not precisely controlled,

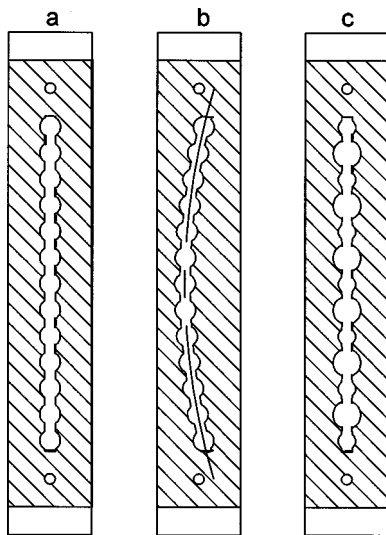


FIG. 3. Injection nozzles forming the gas curtain: (a) one-wavelength ( $\lambda = 6$  mm) perturbation, (b) two-wavelength perturbation “smiley nozzle” ( $\lambda_1 = 6$  mm,  $\lambda_2 \gg \lambda_1$ ), (c) two-wavelength perturbation “two modes” nozzle ( $\lambda_1 = 6$  mm,  $\lambda_2 = 12$  mm).

they are accurately characterized just before the shock-wave interaction.

## B. Diagnostics

To capture images of the evolution of the gas curtain, several combinations of lighting, image acquisition systems, and flow tracers added to the curtain have been used.<sup>12–14,28</sup> In all cases, the flow was illuminated by a horizontal light sheet created by passing laser light (pulsed or continuous) through an optical system involving a cylindrical lens, as shown in Fig. 2. The data quality can be judged by several parameters that depend on the acquisition system. Spatial resolution is dictated by a combination of the resolution of the charge-coupled device (CCD) of the camera and an image intensifier used for gain and/or gating. It is also influenced by the flow tracking fidelity of the tracer.<sup>14,29</sup> Motion blur is minimized by using short-duration pulses from the laser or pulsing the image intensifier (for cw laser illumination). The number of images that can be acquired per event and their minimum spacing in time depends on the number of independent CCD/intensifiers used in the camera as well as the characteristics of the laser system. The mean motion of the evolving gas curtain at the shock’s piston velocity allows the capture of several images on a single CCD, because the curtain is a bright object moving through a dark field. In this case, a minimum time interval between exposures exists to prevent images from overlapping. To reduce the minimum interexposure interval, one could use a combination of several quickly pulsing lasers or a powerful cw laser and a multiple-CCD camera. Multiple CCDs, however, typically mean smaller CCDs and therefore a loss in spatial resolution. Finally, improved dynamic range of the images (i.e., the number of useful brightness levels) is very important for a clear understanding of the mixing processes within the curtain. The main factor determining the dynamic range in an image is the amount of light produced by the illumina-

tion system that is scattered by the gas curtain. The task of producing lighting sufficient to resolve at least 100 brightness levels at exposure durations on the order of  $1 \mu\text{s}$  is difficult for gaseous scatterers. Due to the small amount of light scattered from the gas curtain, the use of an image intensifier is practical, but this happens at the expense of spatial resolution.

In our experiments, we sought an optimal lighting/tracer/camera combination to maximize the spatial and temporal resolution while maintaining an acceptable dynamic range and keeping the error due to flow tracking fidelity of the tracer on the same order as the error due to other limitations in spatial resolution. The paragraphs below describe some of the combinations and their respective advantages and disadvantages.

Budzinski *et al.*<sup>13</sup> used planar laser Rayleigh scattering (PLRS) to measure the concentration of  $\text{SF}_6$  directly.  $\text{SF}_6$  scatters light about six times more efficiently than air. The obvious advantage of this technique is in the ease of direct interpretation of the images in terms of concentration of  $\text{SF}_6$ —flow tracking fidelity of the tracer is not a matter of concern. Unfortunately, PLRS image acquisition requires a huge amount of light and the difficult elimination of unwanted scattering within the facility. With dye lasers producing about 0.2–1.0 J of optical energy per pulse used for illumination and a 512 by 512 digital, thermoelectrically cooled camera employed for image acquisition, only 20–30 levels of brightness could be resolved. The use of two lasers made it possible to acquire two images per event—one of the curtain before the shock arrival and the other a dynamic image. The images resolve  $\text{SF}_6$  concentrations directly and the spatial resolution is adequate. The limitations of this method are in the low temporal resolution (two images from two lasers; difficulties of operating multiple dye lasers) and limited dynamic range.

The addition of tracers to the curtain material makes it possible to produce images with considerably lower levels of illumination, improving the dynamic range and reducing the laser energy required to produce images. Two kinds of tracers have been successfully employed in the experiments—fluorescent gas (diacetyl)<sup>12,28</sup> and glycol fog.<sup>14,29,30</sup> Additional complications one must consider when tracers are employed are the difference in the diffusion time between the tracer and the  $\text{SF}_6$  within the curtain prior to shock impact (since diffusion is not important during the submillisecond time extent of the dynamic event) and the particle lag in the case of droplets. To follow the flow adequately, the particles must be sufficiently small.

In the case of diacetyl gas used as the tracer,<sup>12,28</sup> one planar laser-induced fluorescence (PLIF) image of the perturbed  $\text{SF}_6$ -diacetyl curtain per event was recorded. A single dye laser provided the illumination, and a gated, intensified CCD camera recorded the images. The optical pulse was 200 mJ, however, only about 50% of the light was usable since the pulse duration was  $10 \mu\text{s}$ , and the intensifier was activated for  $5 \mu\text{s}$  during the pulse to reduce motion blur. Nevertheless, at least 50 brightness levels in the curtain were resolved.

Small (i.e., typical dimension of  $0.5 \mu\text{m}$ ) glycol droplets

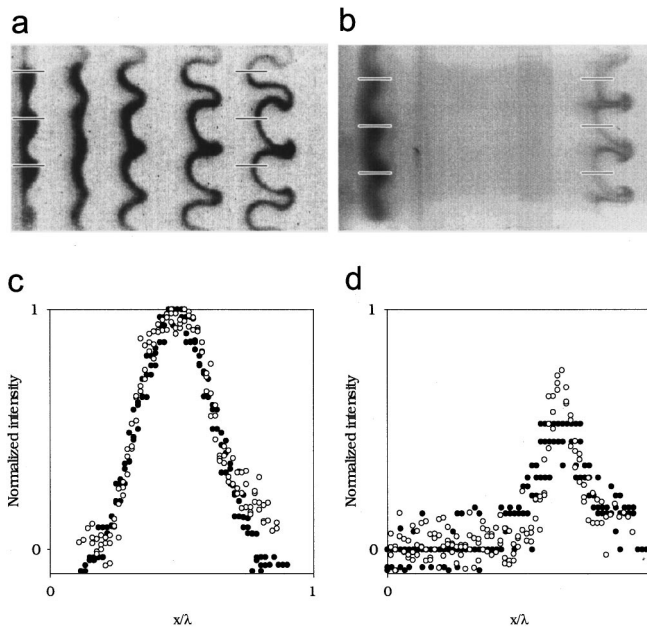


FIG. 4. Initial conditions, dynamic exposure, and normalized intensity profiles at three cross sections through the gas curtain for PLRS and fog scattering: (a) initial conditions and subsequent dynamic exposures with fog, (b) initial conditions and dynamic exposure approximately 400  $\mu$ s after the shock via PLRS (the lines in the images show locations of the sections where intensity profiles were taken), (c) curtain profiles for initial conditions, (d) curtain profiles for dynamic exposure (○—fog, ●—PLRS).

have proven to be a very good tracer. Analysis of their flow tracking fidelity<sup>14</sup> shows that immediately after the passage of the shock, the error due to particle lag is only slightly worse than the CCD resolution limitation. During the instability and mix phases, the tracer follows the flow accurately. Several camera/lighting systems have been employed to record the motion of the SF<sub>6</sub> curtain mixed with this tracer.

The first of these systems<sup>14</sup> uses an intensified, gated camera (Hadland Photonics SVR) with a single 1134 by 437 CCD array. During each event, nine exposures are taken, the first recording the initial condition of the curtain before the shock arrives. The light source is a 1 W Ar<sup>+</sup> cw laser. The subsequent exposures are produced by triggering the intensifier, with the exposure duration being 2  $\mu$ s and the optical energy per exposure 2  $\mu$ J. The dynamic range of the images is 120 levels of brightness or better. The combination of the enhanced scattering from the fog droplets and the intensified camera improves the dynamic range of the images while using five orders of magnitude less optical energy per exposure than the PLRS experiments.<sup>13</sup> Comparison of the PLRS results with the images of the curtain with fog droplets supports the notion that the fog does indeed track the SF<sub>6</sub> well. Figure 4 shows superpositions of three normalized intensity profiles of the initial conditions and at times near 400  $\mu$ s after the shock interaction for two experiments—PLRS and the curtain with fog. Figure 5 shows a similar comparison for the pixel intensity histograms in the curtain. In Figs. 4 and 5 intensity was normalized by subtracting the background pixel value and dividing the result by the dynamic range of the image. As Fig. 4 shows, both the observed morphology and the intensity profiles through the initial conditions and dynamic exposure are extremely similar in the images acquired via PLRS and with the fog tracer, providing additional confirmation that the fog accurately tracks with the flow. Histograms of the normalized intensity of PLRS and fog images show similar tendencies in their evolution (Fig. 5). The initial condition has two peaks—one at normalized intensity 0.2 corresponding to ambient air, the other (less prominent) at normalized intensity at and above 0.7 corresponding to 60% sulphur hexafluoride in the gas curtain. In the dynamic images, the second peak in the histogram is eroded. The amount of detail that can be recovered from this

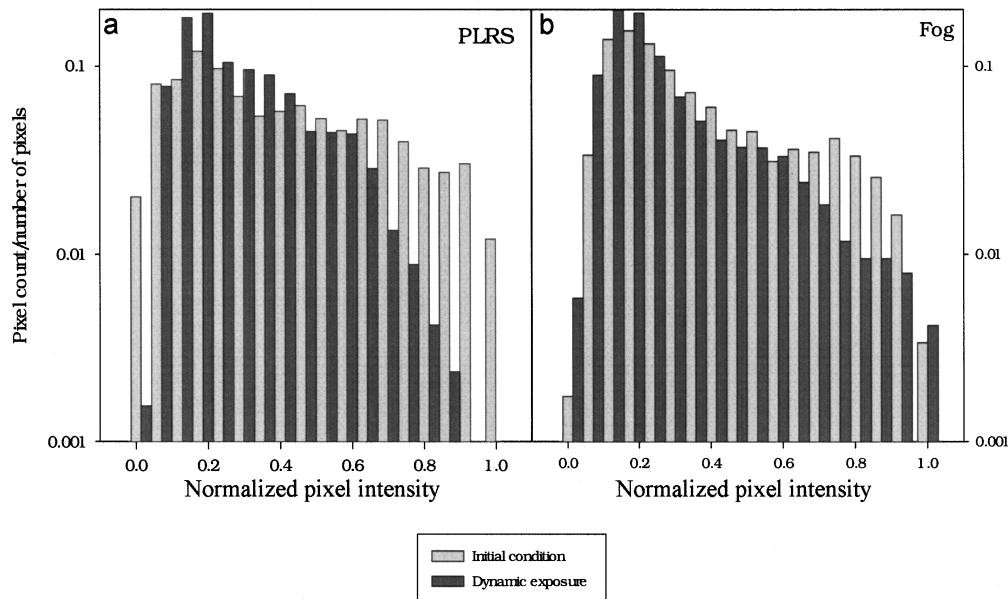


FIG. 5. Pixel brightness histograms comparison for SF<sub>6</sub> and fog scattering: (a) PLRS, (b) fog.

histogram comparison is limited by the low dynamic range of PLRS images. The wider dynamic range of fog images makes it possible to do a more thorough analysis of the histograms. Such an analysis is presented in Sec. IV.

An alternative system employed in conjunction with the fog tracer<sup>29</sup> uses an unintensified, thermoelectrically cooled 512 by 512 camera (Photometrics) and a Positive Light Merlin Nd:YLF laser pulsing at 5 kHz. This system allowed the acquisition of only 4 images per event, but with excellent spatial resolution and dynamic range (more than 200 brightness levels). The optical energy per pulse is 3 mJ.

Finally, to maximize the temporal resolution, we used an eight-channel, intensified Hadland Photonics Imacon 468 camera with the 1 W Ar<sup>+</sup> cw laser as the light source.<sup>30</sup> The spatial resolution of each CCD in this camera (586 by 385) is somewhat lower than that of the single-CCD devices and is further reduced through the use of the microchannel plate (MCP) intensifier at high gain. The presence of eight intensified CCDs allows the recording of up to 32 images per event (up to 4 images per channel), with the intervals between the images as low as 20  $\mu$ s. This reveals the features of the curtain evolution that have not been experimentally observed before, such as nonmonotonic growth of the curtain width due to phase reversal.

In each experimental setup, there are three sources of random errors and one source of systematic errors. Random errors stem from limitations in the (1) dynamic range and (2) spatial resolution of the CCD, as well as from (3) intensifier noise in the case when the intensifier is used. The source of systematic error is the tracer lag during the shock acceleration, but our earlier work<sup>14</sup> estimates the spatial extent of this lag to be on the order of the pixel resolution of the CCD (0.1 mm for the images quantitatively analyzed in this paper), so random errors due to CCD limitations are more important. The dynamic range of the images varies from 30 levels of brightness for the Imacon 468 to 120 for Hadland Photonics SVR camera and 200 for Photometrics camera. The rms estimate of the background noise introduced by the intensifier (SVR camera) is 4.5 brightness levels, thus the rms random error in brightness measurements is 3.75% per pixel. In the graphs presented in this paper the influence of random error is reduced even further, because the graphs show results of spatial averaging over a considerable number of pixels.

As the fog tracer proved to be an excellent choice in terms of optimizing the spatial and temporal resolution of the system, all the data discussed in the following sections of this paper are of the fog-tracer type. Prior to describing the results of our analysis, we must make some comments regarding the interpretation of tracer visualization results in general and the specifics of our experiment. The most typical tracer visualization technique, streakline visualization, is known to produce results that can be misleading in the interpretation of time-dependent flows: for instance, the roll-up of a streakline does not necessarily imply the presence of a vortex.<sup>31</sup> Thus one must exercise caution when reconstructing the flow from a scalar tracer visualization. The shortcomings of scalar tracers are described in the review by Ottino.<sup>32</sup> However, our technique employing a passive scalar tracer is in some aspects better than a traditional streakline visualiza-

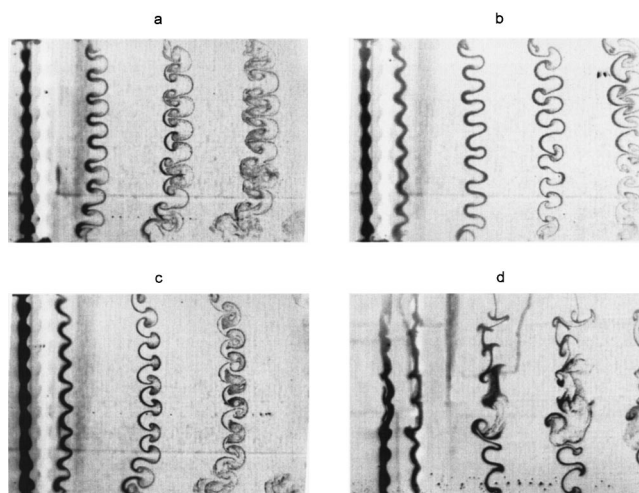


FIG. 6. Gas curtain morphologies evolving from single-mode perturbations: (a) upstream mushrooms, (b) sinuous mode, (c) downstream mushrooms, (d) irregular morphology. Nd:YLF laser pulsed at 5 kHz (200  $\mu$ s between pulses) used for illumination, glycol droplets employed as tracer. The image shows nearly the entire spanwise extent of the tube.

tion because it provides additional physical information about the flow. The tracer is injected and advected with the gas curtain, thus tracking the SF<sub>6</sub> concentration field—a relevant physical property of the flow. It also helps that in our experiments vorticity is originally generated only in the presence of density gradients. This means that most of the tracer-free parts of the images are also vorticity free, and we largely avoid one of the major pitfalls of generic streakline visualization—the inability to see a vortex if no tracer gets into it. Moreover, we have knowledge of the overall vortex structure of the flow from the initial curtain geometry, because vorticity production is baroclinic. With this knowledge, we can provide a more thorough interpretation of the flow images than that possible with streakline information only.

A cylindrical lens is employed to produce the laser sheet, so the intensity of the illumination in the sheet falls off toward the edges, as seen in the experimental images presented in this paper. The nonuniformity was taken into account during the processing of the data, as described in Secs. IV A and IV B.

### III. QUALITATIVE COMPARISON OF FLOW MORPHOLOGIES

We briefly describe the flow morphologies observed in the experiments, starting with the single-mode perturbations and moving on to multiple modes. Several examples of the instability development in the curtain with a single-mode perturbation on the nozzle are shown in Fig. 6. These images were acquired with the 512 by 512 CCD array camera/pulsed Nd:YLF laser/glycol droplet tracer combination described in Sec. II. In each of the images, the direction of the shock is from left to right and the first (overexposed) image of the curtain from the left shows the initial conditions of the curtain. The time delay between the shock reaching the curtain and the first dynamic exposure is subject to substantial jitter

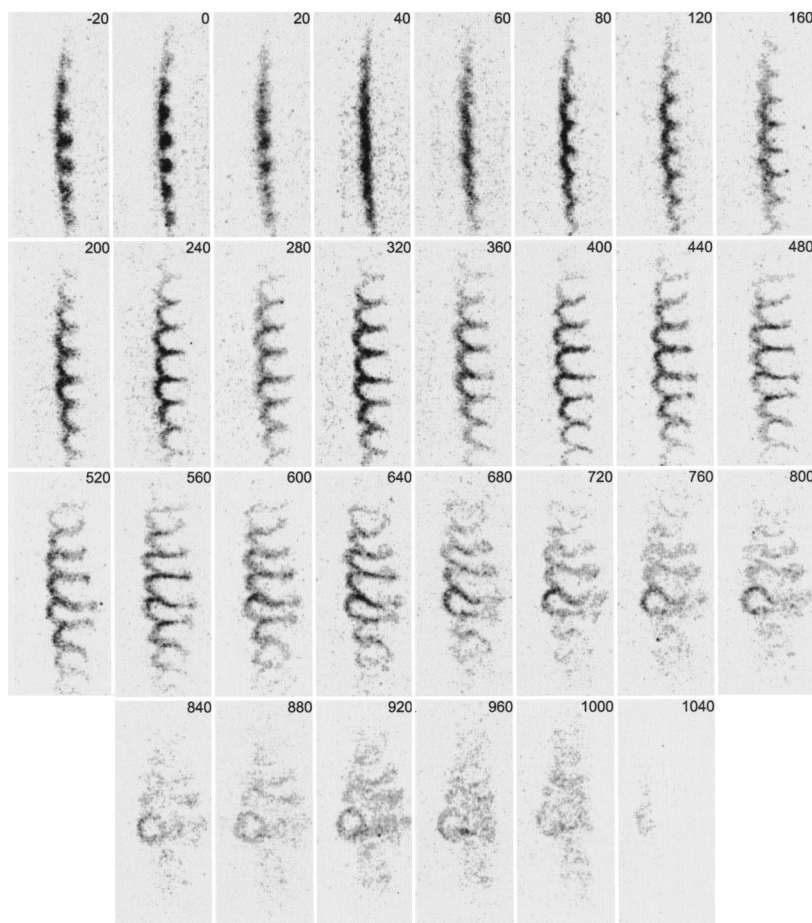


FIG. 7. Gas curtain morphologies evolving from two-mode initial perturbation produced by the “smiley” nozzle. Images of the  $\text{SF}_6$  curtain with glycol fog are acquired with a multi-CCD Imacon 468 camera. A 1 W  $\text{Ar}^+$  cw laser was used for illumination. Exposure duration of  $10 \mu\text{s}$  and exposure delays in microseconds respective to shock arrival are labeled. The spanwise extent of the imaged area is 50 mm.

(50–150  $\mu\text{s}$ ). Intervals between the subsequent dynamic exposures are 200  $\mu\text{s}$ . The distance downstream (left to right) from the initial exposure (left edge) equals the shock piston velocity times the exposure delay from the time of shock interaction with the curtain.

Small variations in the initial shape of the curtain produce slightly different initial conditions for each shot. This emphasizes the need to obtain many images from each event. Perturbations on the upstream side of the curtain start growing immediately after the shock passes, while the downstream interface perturbations undergo phase inversion first. The combination of the different behavior of the interfaces with the variations of the initial conditions produces different patterns in the process of perturbation growth.

If the perturbations on the upstream side of the curtain have significantly greater amplitude than those on the downstream side [Fig. 6(a)], the upstream mushroom flow pattern develops, with the “mushroom caps” aligned with the peaks of the perturbation of the upstream interface. Initial conditions with the perturbation of the downstream interface being more prominent [Fig. 6(c)], produce the downstream mushroom pattern. The downstream mushrooms form after the downstream interface undergoes phase inversion, and their growth is delayed in comparison with the upstream mushrooms.<sup>14</sup> In this case, the mushroom caps are aligned with the valleys of the initial perturbations. For a relatively symmetric initial condition with upstream and downstream perturbation of the same order, the phase inversion of the

downstream interface results in the curtain acquiring a sinusoidal shape and evolving symmetrically for some time [Fig. 6(b)].

In the case of the single-mode initial perturbation, there is relatively little interaction between the wavelengths in the early to intermediate stages of the curtain evolution (times up to 400  $\mu\text{s}$  after the shock), and the flow morphologies described above can coexist.<sup>14</sup> Figure 6(d) shows an example of irregular initial conditions (containing more than one mode) producing downstream mushrooms, upstream mushrooms, and less identifiable structures in the evolving curtain. As will be shown later in this paper, the initial conditions with a single prominent spatial scale (perturbation wavelength,  $\lambda$ ) also evolve into flows with scales both larger and smaller than  $\lambda$ , which may be indicative of the onset of turbulence.

In order to focus on the interaction between the different scales important in the process of transition to turbulence, we employ nozzles imposing multiple-mode initial perturbations upon the curtain. Thus it becomes possible to focus on the interaction between different scales from the very beginning of the experiment. Figures 7–9 show some of our observations for such perturbations. Unlike the images illustrating single-mode flow morphologies, Figs. 7–9 were acquired with a multi-CCD camera. Intervals between exposures were varied from 20  $\mu\text{s}$  at early times to 40  $\mu\text{s}$  at later times. Exposure delay times with respect to the shock interaction with the curtain are shown in Figs. 7–9. Each of the images

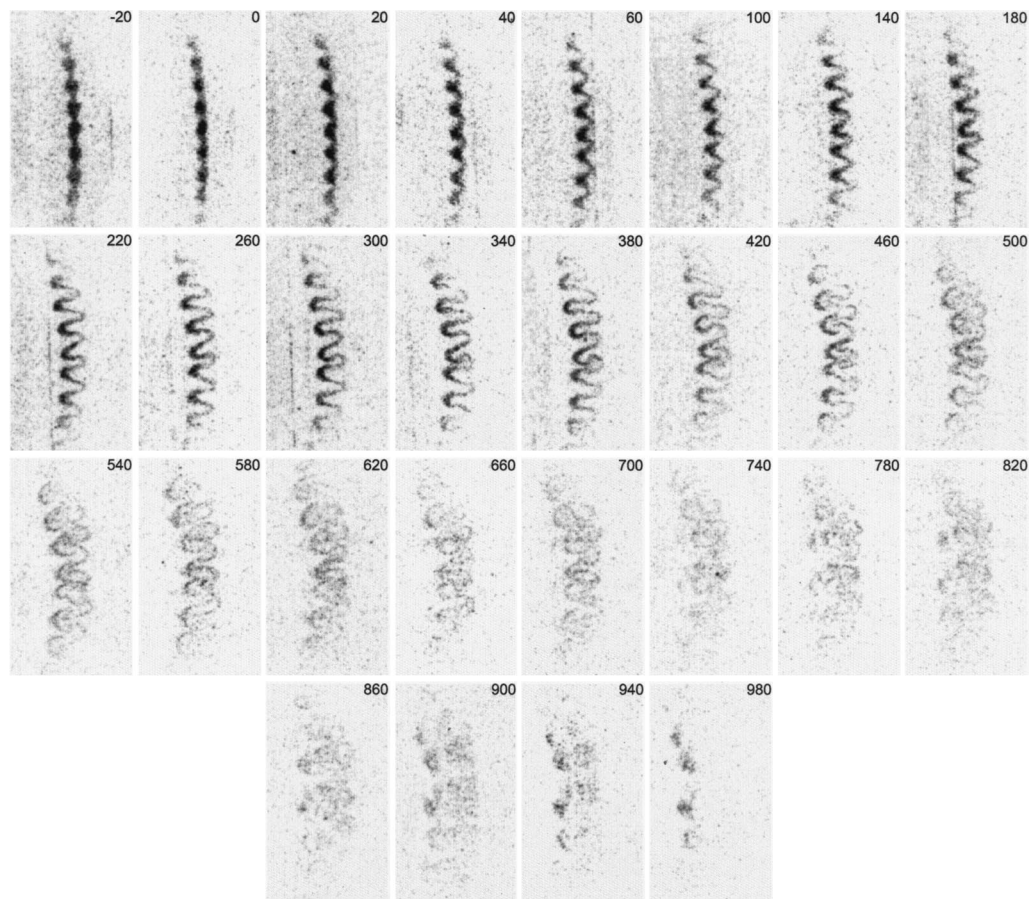


FIG. 8. Gas curtain morphologies evolving from two-mode initial perturbation produced by the “smiley” nozzle turned 180°. Images of the SF<sub>6</sub> curtain with the glycol fog are acquired with a multi-CCD Imacon 468 camera. A 1 W Ar<sup>+</sup> cw laser is used for illumination. An exposure duration of 10 μs and exposure delays in microseconds respective to shock arrival are labeled. The spanwise extent of the imaged area is 50 mm.

represents a typical evolution pattern observed in multiple experiments.

Figure 7 shows evolution of the gas curtain extruded through the “Smiley” nozzle [Fig. 3(b)] with the crest of the large-wavelength perturbation oriented toward the shock. The flow is characterized by two features not present in the single-mode experiments. First, the large-wavelength perturbation appears to decrease in amplitude rather than grow. Second, there is enhanced growth of the small-wavelength perturbation near the location of the crest of the large-wavelength perturbation.

It is interesting that by changing the orientation of the “Smiley” nozzle by 180°, we can reverse the effect of large- and small-amplitude perturbation interaction (Fig. 8). The curvature associated with the large-wavelength perturbation is increasing, while the local mixing layer width of the curtain in the late (after 800 μs) images in Fig. 8 is smaller than in Fig. 7. This effect has been observed in many experimental events. The increase or decrease of interface curvature on the large scale is caused by the deterministic interaction of the vortex pairs deposited by the passage of the shock wave. By modifying the initial conditions and the subsequent regular flow we can also increase or decrease the growth of the apparently disordered structures at the smallest scale.

This possibility is further elucidated when we consider another example of interaction between perturbations of two

wavelengths presented in Fig. 9. In this case, the initial perturbation contains two wavelengths,  $\lambda_1 = 6$  mm and  $\lambda_2 = 12$  mm [Fig. 3(c)]. Growth of the perturbation associated with  $\lambda_2$  appears to suppress the growth of the  $\lambda_1$ -associated features. However, from clean (i.e., no “unwanted” modes) initial conditions, a strongly disordered flow develops within the limited extent of the test section. This differs from single-mode flows such as those depicted in Figs. 6(a)–6(c).

#### IV. QUANTITATIVE ANALYSIS PROCEDURES AND RESULTS

Two processes important for the phenomenological characterization of the mixing transition are: the mixing of the curtain material with the surrounding air masses that should be considerably enhanced by turbulence (Sec. IV A), and the formation of spatial scales both larger and smaller than the scale of the initial perturbation (Sec. IV B).

##### A. Intensity histograms of diffuse interfaces

Measured intensities appearing on the experimental image are directly related to the mole fraction of SF<sub>6</sub> (and therefore to the density of the fluid) in the region of the flow representing the pixel.<sup>13,20</sup> Therefore, the histograms of the

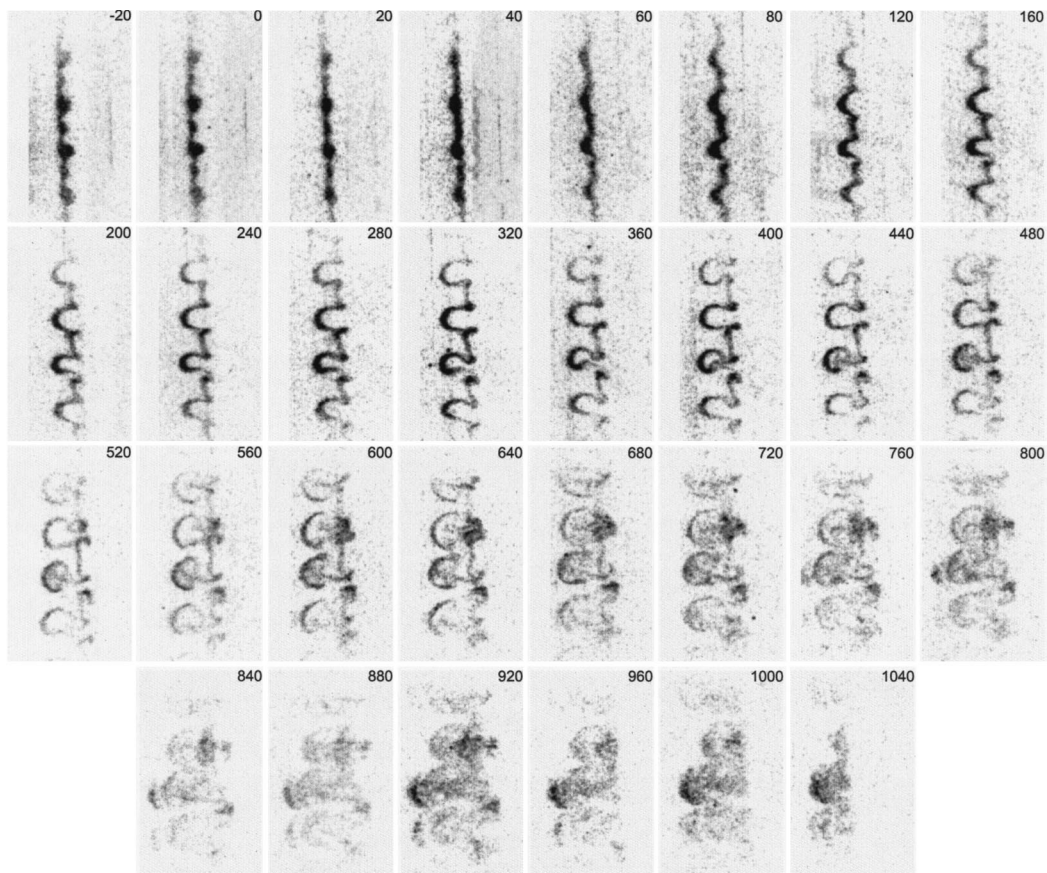


FIG. 9. Gas curtain morphologies evolving from two-mode initial perturbation produced by the “two modes” nozzle. Images of the  $\text{SF}_6$  curtain with the glycol fog are acquired with a multi-CCD Imacon 468 camera. A 1 W  $\text{Ar}^+$  cw laser is used for illumination. An exposure duration of 10  $\mu\text{s}$  and exposure delays in microseconds respective to shock arrival are labeled. The spanwise extent of the imaged area is 50 mm.

intensity field for each dynamic exposure can be used to analyze the mixing occurring between  $\text{SF}_6$ /fog and air within the flow.

Consider two distinct substances in a geometry similar to that of the gas curtain described in this study (i.e., a thin layer of highly scattering material sandwiched between regions of material that do not scatter light). An intensity profile of this would be shaped like a top hat, with the corresponding histogram having two peaks. The pixels from the highly scattering region would read uniformly at high values, while those pixels from other regions would ideally read zero. If the system was stirred vigorously and the substances allowed to mix, this top-hat histogram would erode as more pixels took on values between the original two extremes depending on the fraction of the two substances in the volume represented by the pixel. In this way, mixing can be visualized by a histogram analysis.

The interpretation of such an analysis is complicated when the two substances diffuse into each other readily (e.g., gases—as in this study) and their initial states are not entirely pure. One interest of this study is to understand the mixing due to the convective motions induced by the Richtmyer–Meshkov instability. Therefore, we must distinguish between the mixing occurring before shock impact due to diffusion and mixing due to the late-time instability motions. After the shock interaction the contribution of diffu-

sion to mixing is unimportant, so diffusive mixing is relevant only in producing the initial conditions.

Insufficient sampling frequency may cause problems in histogram analysis. Figure 10 displays a generic Gaussian sampled at several “frequencies” and the resulting histograms. The Gaussian is selected to mimic the intensity profile occurring in the initial conditions prior to shock impact (Fig. 4c, also see Baltrusaitis *et al.*<sup>20</sup>). In this case, the ordinate of the first part of Fig. 10 represents intensity while the abscissa is the streamwise spatial axis. For an image that provided ten samples across this profile (the large, closed circles) the histogram is exceedingly spiky. Images with progressively more samples across the profile converge to a double-peak histogram similar to that generated by two unmixed substances. For sufficient sampling “frequency,” the histogram produces peaks from regions of zero gradient of intensity with the height of the peak related to the breadth of the region. In this case, the second peak represents the second “unmixed” substance. We know from earlier studies,<sup>13,20</sup> however, that the fluid at the center of the curtain prior to shock impact is approximately 60% mole fraction  $\text{SF}_6$ .

Figure 11 shows an image of a sinuous mode event as well as the evolution of the intensity histogram for each exposure. The extent of the bounding box containing the exposure is determined as follows. The vertical boundary is set to

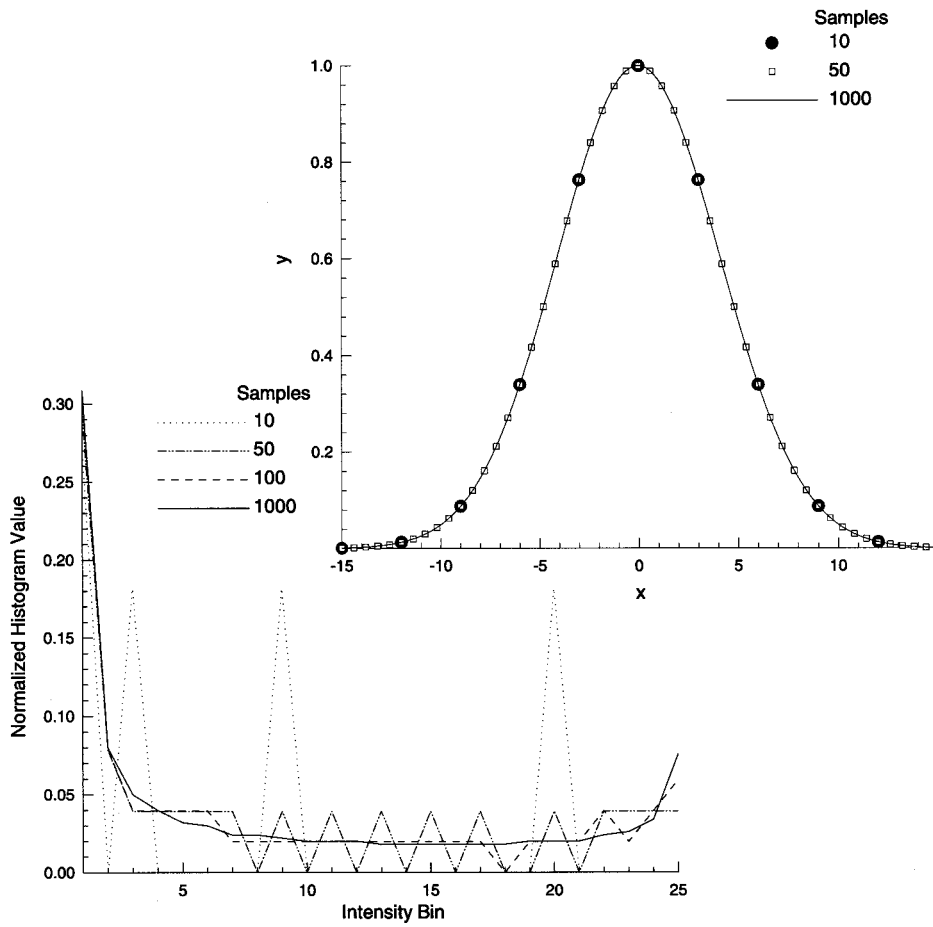


FIG. 10. Convergence of histograms of a generic Gaussian signal with different samplings.

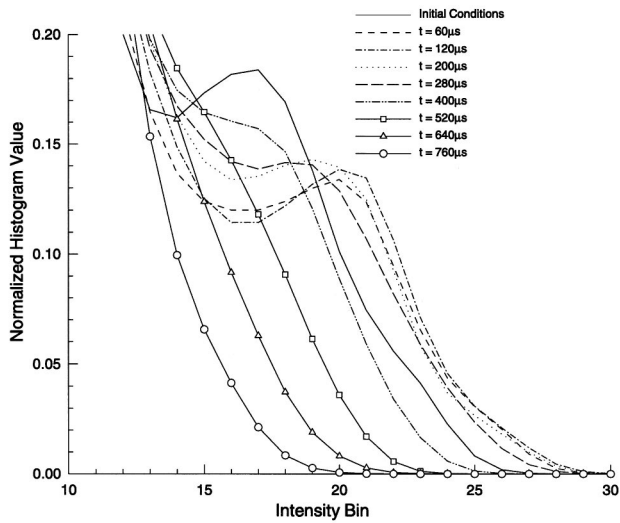
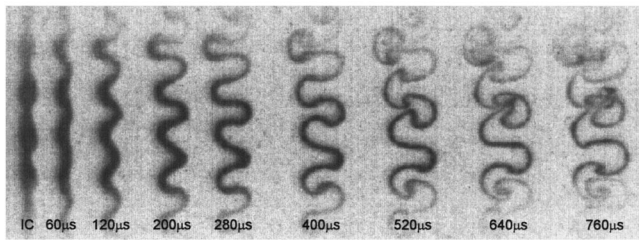


FIG. 11. Histogram evolution without appreciable mixing transition.

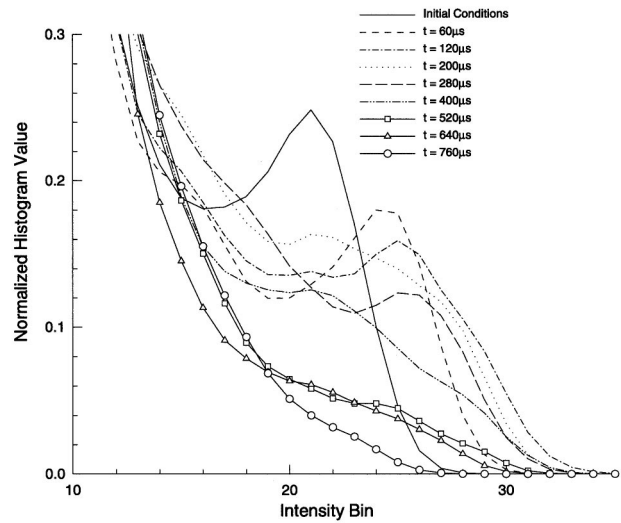
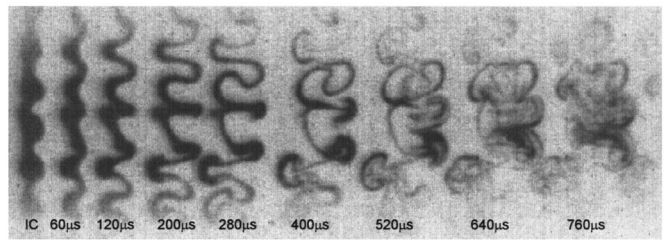


FIG. 12. Histogram evolution with mixing transition.

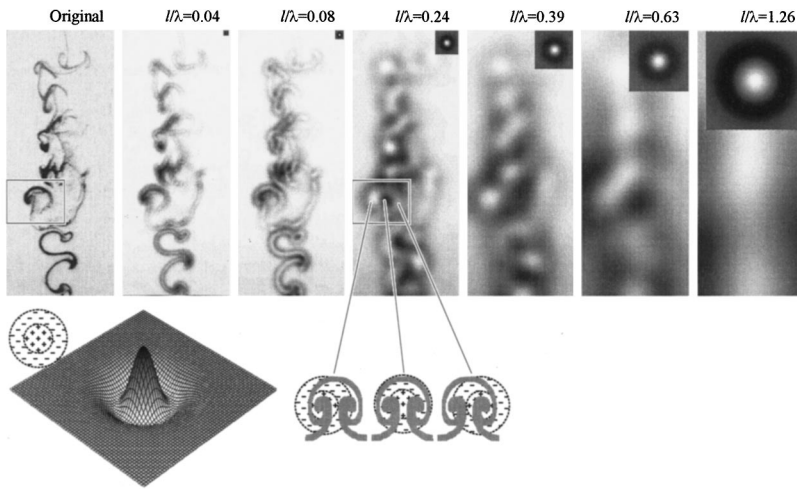


FIG. 13. Mexican hat wavelet filtering at different dilations applied to an image of the perturbed gas curtain. Dilatation scales  $l$  nondimensionalized by characteristic wavelength  $\lambda$  are labeled. Inserts show dilated wavelet. The schematic at the bottom illustrates how mushroom caps produce a regular pattern in the filtered signal. The value  $l/\lambda = 1/2$  corresponds to the wavelet size matching the initial perturbation wavelength.

remove the edges where the light sheet intensity starts to fall off. This setting is the same for all exposures. The horizontal span of the bounding box containing the image of the curtain varies between the exposures, so that late-time exposure computation uses more points. In order to avoid undersampling errors described in the previous paragraph, we apply bilinear interpolation between pixels before computing the histogram. The typical number of samples averaged to produce each point in the plot is 700. Thus the error due to intensifier noise (3.75% per pixel) can be estimated as 0.14%. In the center of the initial conditions (intensity bin 17, representing the least mixed part of the curtain), a peak corresponds to the “unmixed”  $\text{SF}_6$ . The dominant peak at low intensity in the histogram representing unfogged air is not shown in Fig. 11. After shock interaction, the peak associated with the curtain fluid in the initial conditions moves to higher intensity levels due to compression. From the image, no turbulent mixing is visually apparent within the test section. The evolving histogram shows a smooth decay of the peak associated with the curtain fluid, due purely to straining effects on the curtain. We suggest that this is a signature of “weak mixing.”

Contrast this with the evolution of the histogram associated with a flow field in which significant turbulent mixing is apparent (Fig. 12). In this case, multiple, irregular wavelengths characterize the initial conditions of the interface. This leads to rapid mode coupling and transition into a highly disordered state. At early times (before mode coupling), the evolution of the histogram is qualitatively similar to that of Fig. 11. In this region the straining of the curtain fluid reduces the concentration of the curtain material, eroding the peak. One can see that in this way, interpolation-histogram techniques can be used to study the mixing associated with scales smaller than an arbitrary scale—instead of being limited to the sampling of the image. After the fifth dynamic exposure ( $\sim 400 \mu\text{s}$ ), an abrupt decay of the peak associated with the curtain fluid occurs. Between the fifth and sixth dynamic exposures, we see that the interacting structures of the flow have begun to impact each other and produce much more disorder. This sudden transition in the evolution of the histogram signifies a sudden increase in the mixing of the flow field. Approximately 40% of the curtain material mixes during the  $120 \mu\text{s}$  interval between the fifth and sixth dynamic exposures. We suggest that it indicates an

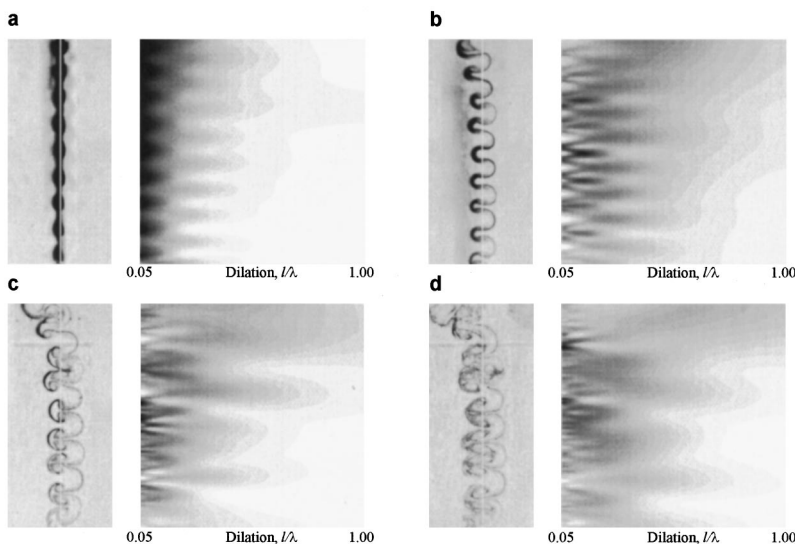


FIG. 14. Mexican hat wavelet transform of the upstream mushroom image sequence. The vertical coordinate (translation) corresponds to the vertical coordinate in physical space, the horizontal coordinate is the non-dimensionalized wavelet dilation  $l/\lambda$ . The value  $l/\lambda = 1/2$  corresponds to the wavelet size matching the initial perturbation wavelength. Two-dimensional wavelet transforms at all dilations are taken along the centerline of the curtain, marked by a thin white line in the curtain images. The darkest spots in the transform images mark amplitude peaks, white is zero amplitude.

abrupt mixing transition similar to that described for the Kelvin–Helmholtz instability.

## B. Wavelet analysis

Besides mixing, transition to turbulence is characterized by the formation of multiple scales in the flow.<sup>33</sup> To analyze the evolution of scales, we employ the wavelet transform that has been successfully applied to space-scale analysis of fluid flows.<sup>22–24</sup>

The standard procedure for constructing wavelet transforms is described by Farge.<sup>22</sup> It begins with choosing the mother wavelet function  $\psi(\mathbf{x})$  satisfying the admissibility condition, which for an integrable function simply requires having zero mean. For practical purposes, the mother wavelet should also be well-localized in both physical and Fourier spaces.

By translating, rotating, and dilating the mother wavelet  $\psi(\mathbf{x})$ ,  $x \in \mathcal{R}^n$ , we generate the family of wavelets:

$$\psi_{l\mathbf{x}'\theta}(\mathbf{x}) = l^{-n/2} \psi\left(\Omega^{-1}(\theta) \frac{\mathbf{x} - \mathbf{x}'}{l}\right), \quad (1)$$

where  $l$  is the dilation parameter,  $\mathbf{x}'$  is the translation parameter, and  $\Omega$  is the rotation matrix. Then the general expression for a wavelet transform of a scalar function  $f(\mathbf{x})$  can be written in the form

$$\tilde{f}(l, \mathbf{x}', \theta) = \int_{\mathcal{R}^n} f(\mathbf{x}) \psi_{l\mathbf{x}'\theta}^*(\mathbf{x}) d^n \mathbf{x}, \quad (2)$$

where  $\psi_{l\mathbf{x}'\theta}^*$  represents the complex conjugate of  $\psi_{l\mathbf{x}'\theta}$  from Eq. (1).

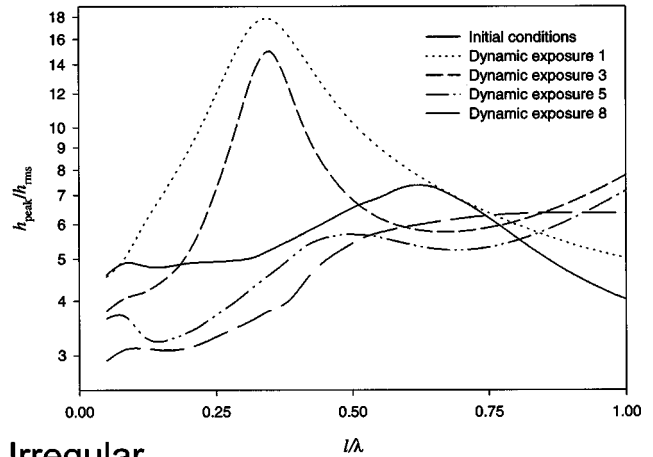
In our case,  $n=2$  and  $f(\mathbf{x})$  is the local intensity of the digital image which, as we have shown, grows monotonically with the concentration of  $\text{SF}_6$ .

To construct the transforms employed in the analysis presented below, we employed the real-valued and rotationally invariant Mexican hat wavelet, which was first applied to the studies of turbulent flows by Everson *et al.*,<sup>24</sup>

$$\psi(\mathbf{x}) = (1 - |x|^2) e^{-|x|^2/2}. \quad (3)$$

Our implementation of the wavelet transform code is fairly straightforward, since it is applied to relatively small domains (characteristic size 100 by 400), thus making code efficiency relatively unimportant. To provide reasonable transform values near the image boundaries, the exposures of the gas curtain are padded with pixels of background value in the direction of the shock propagation (left and right boundaries). In the direction parallel to the gas curtain (top and bottom boundaries), we employ reflections of the original image for padding. In the following paragraphs, we use the terms “wavelet filter” or “filter” to denote application of wavelet transform at a fixed dilation value  $l$  and translating it across the entire image plane. This operation is equivalent to convolution of the original signal with the dilated mother wavelet function. In the data presented below, the maximum scale of the filter does not exceed  $\lambda$ . The lighting nonuniformity inside the laser sheet becomes relevant on scales  $\sim 4\lambda$ , thus it does not interfere with the wavelet detection of coherent features.

## Sinusoidal



## Irregular

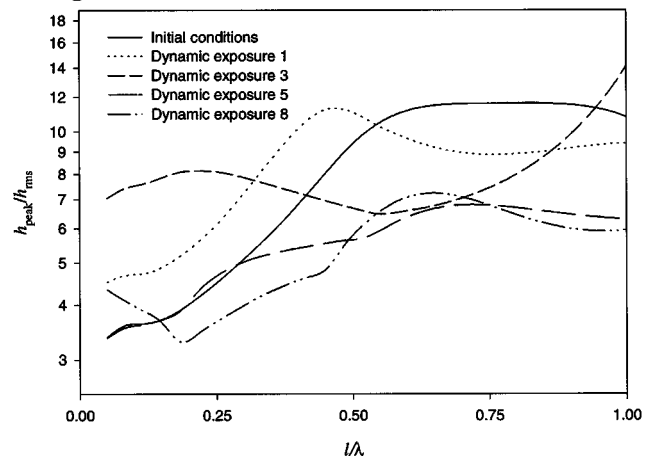


FIG. 15. rms values of wavelet transform amplitude vs dilation for the data sets shown in Figs. 11 and 12. rms transform values are nondimensionalized by rms averages of the corresponding maps. The value  $l/\lambda = 1/2$  corresponds to the wavelet size matching the initial perturbation wavelength.

The Mexican hat wavelet is particularly suitable for the analysis of the gas curtain flow, as one sees in Fig. 13. It shows the results of applying the Mexican hat filter to an image of the perturbed gas curtain [the third dynamic exposure in Fig. 6(d), multiple-wavelength irregular initial conditions] at several values of dilation  $l$ . The values of  $l$  in the labels are normalized by the wavelength  $\lambda$  imposed on the initial condition by the single-mode nozzle. Inserts in the images show the size of the dilated wavelet. For wavelengths showing the regular mushroom pattern (the lower part of the images), small dilations ( $l/\lambda \sim 0.1$ ) of the wavelet filter result primarily in edge enhancement combined with smoothing. Intensity peaks (darker) are associated with small-scale structures (e.g., the small downstream mushroom cap near the bottom of the original image or the irregular shapes near the center).

As the value of  $l$  increases, the appearance of the filtered image field changes. A simple regular structure present in parts of the filtered image is associated with the mushroom pattern, which shows the value of using this particular wavelet in analysis of flows with regular structures, e.g., vortex pairs. When the characteristic size of the dilated Mexican hat

is close to that of the mushroom, filtering transforms the mushroom shape into a combination of two positive peaks (bright) and one negative peak (dark). Compare, for instance, the windowed regions in the original image and in the image corresponding to  $l/\lambda = 0.24$  in Fig. 13. The sketch at the bottom of Fig. 13 clarifies the origins of this pattern. When the arc of the mushroom cap is aligned with the negative-valued “brim” of the hat, the convolution integral is negative. When the “peak” of the hat is aligned with one of the concentrations of the curtain material, the integral is positive. For regular flow morphologies, the characteristic scale of the mushrooms is close to  $\lambda/2$ . Correspondingly, the wavelet filter with the scale  $l/\lambda = 0.5$  should produce regular patterns when applied to regular morphology images. The sensitivity of wavelets to regular patterns in the flow has been emphasized by Farge<sup>22,23</sup> and exploited by Vorobieff and Rockwell<sup>25</sup> for a “topological decomposition” of the turbulent flow: applying an appropriate wavelet to correlate with a specific pattern in the flow and to produce a matching but simpler pattern in the transform plane.

For high values of  $l$  ( $l/\lambda = 1.26$  in Fig. 13) the regular pattern associated with the single-mode wavelength can no longer be distinguished, though a positive peak is present in the general region of the curtain in the filtered plane. At high values of  $l$ , the wavelet filter is sensitive to features of scales greater than  $\lambda$ .

With this notion of the way wavelet filtering works, let us apply Mexican hat transform to the gas curtain images shown in Fig. 6(a) (upstream mushrooms). Figure 14 shows transforms corresponding to different stages of the evolution of the curtain. Transform images were produced as follows. Along the centerline of the curtain (the white line in Fig. 14), a two-dimensional wavelet transform of each exposure was computed at a range of dilations from  $l/\lambda = 0.05$  to  $l/\lambda = 1$ . Then the results were plotted as two-dimensional intensity maps of the transform with dilation as the horizontal coordinate and vertical translation (corresponding to the vertical coordinate in the physical domain) as the vertical coordinate. Darker regions in the maps are transform intensity peaks, while white corresponds to zero.

What is the signature of the flow evolution in transform space? The initial condition transform map [Fig. 14(a)] exhibits a regular structure associated with the varicose shape of the curtain. This structure is  $\lambda$  periodic in the vertical direction for dilations  $l/\lambda < 0.5$ . Low dilations ( $l/\lambda \sim 0.1$ ) are characterized with high amplitudes of signal, likely due to the fact that at these scales the size of the “peak” of the Mexican hat closely matches the curtain thickness. At values higher than  $l/\lambda = 0.5$ , no features can be distinguished in the transform map.

The transform map of the first dynamic exposure [Fig. 14(b)] is radically different. First, it is no longer dominated by peaks at low  $l/\lambda$ . Second, the map is highly regular for  $l/\lambda$  values up to 0.5. Its periodicity in the vertical direction is  $\lambda$  between  $l/\lambda \sim 0.25$  and  $l/\lambda \sim 0.5$  and is due to the overall sinuous shape of the curtain, or the mushroom “caps.” At lower scales,  $\lambda/2$  vertical periodicity can be associated with mushroom “stems” intersecting the centerline. The part of the map at  $l/\lambda > 0.5$  remains practically devoid of structure.

In the map of the second dynamic exposure, Fig. 14(c), we continue to observe  $\lambda$  and  $\lambda/2$  periodicity caused by the presence of the mushrooms. However, a more complex structure emerges at low dilation scales, perhaps  $\lambda/4$  periodic. One can also notice that mushrooms showing some evidence of mode coupling in physical space (the third wavelength from the top) produce a ridge in the transform map extending to  $l/\lambda \sim 0.75$ . Formation of features in the large-dilation area of the map indicates the presence of physical scales larger than that of the initial perturbation.

The signature of the mushrooms in the third dynamic exposure [Fig. 14(d)] is much weaker, while structures both on the small and large scale grow. This pattern of evolution is suggestive of developing turbulence. It can also be implied that the small and apparently irregular features on the lower end of the dilation range formed as the result of a cascade from structures of a spatial scale  $\lambda$  [Figs. 14(a), 14(b),  $l/\lambda \sim 0.3$ ] to structures of scale  $\lambda/2$  [Fig. 14(b),  $l/\lambda \sim 0.15$ ] and on to spatial scale on the order of  $\lambda/4$  [Fig. 14(c), *d*,  $l/\lambda \sim 0.1$ ]. The limited resolution of the images may not allow accurate quantification of this transition for smaller scales, however, by means of wavelet transform we do get some insight into the properties of the scale evolution.

Additional quantitative information can be provided by plotting the graphs of the ratio between peak transform amplitude versus dilation for different times (Fig. 15). In each map, we nondimensionalize the peak value by the rms amplitude. The amplitude of  $\tilde{f}(l, \mathbf{x}', \theta)$  corresponds to the local “energy density” of the signal. Thus these plots can be interpreted as mean “energy densities” versus scale. The accuracy of the graphs is limited by the pixel resolution of the system—1.5%  $\lambda$ . The upper plot in Fig. 15 shows the results for the image used in Fig. 11 (sinuous morphology), while the lower plot corresponds to the image and histograms of Fig. 12 (irregular morphology). The decrease of the overall transform peak/rms ratio with time can be explained by the influence of several factors—diffusion of the curtain material, loss of features too weak to be detected above the background value or too small to be resolved.

In both cases, the initial conditions are characterized by an amplitude peak near  $l/\lambda = 1/2$ —dilation corresponding to the wavelet size matching the initial wavelength. For the irregular case, this peak is noticeably wider, showing that the initial condition contains a wider range of scales. It is interesting that the subsequent plots for the first dynamic exposure show prominent peaks at half the initial wavelength. This transformation can be explained by the following. Initially, the maxima in the transform plane are due to the “peak” of the Mexican hat aligning itself with the varicose bulges in the curtain. As the downstream side of the gas curtain undergoes phase inversion and the curtain becomes sinuous, the bulges disappear. Now the features most distinguishable in the transform plane are the sinuous “humps” of the curtain developing into mushroom caps, and their characteristic size is initially half the perturbation wavelength.

Plots for the third dynamic exposure are considerably different for the sinuous and irregular morphologies. The sinuous morphology plot still has the peak at the mushroom

cap size, while the irregular plot has a local maximum at a somewhat smaller dilation and shows strong growth of both large and small scales. Here it must be mentioned that some of the features of the third dynamic exposure, such as the high peak transform values at large dilations, may be due to the motion of the curtain material in the out-of-plane direction. Growth of the large scales, indicative of mode coupling, is also apparent in the sinuous morphology plot.

As the sinuous morphology (dynamic exposure 5) continues to develop, the peak corresponding to the mushroom cap size moves toward larger scales, following the cap growth. The growth of amplitude at small scales is also apparent, both in this plot and in the fifth dynamic exposure for the irregular morphology. The latter plot is also quite similar to the plot for the eighth dynamic exposure in the sinuous case—a peak at small scales and relatively high values for  $l/\lambda > 1/2$ . The shape of these plots, with the well-defined peaks produced by the coherent structures (mushrooms) eroding, indicates the increase of disordered features in the flow. The irregular morphology advances toward the disordered state much faster, and the steps in the time evolution of the peak amplitude/rms plots are roughly consistent with the steps in the time evolution of the corresponding histograms.

Finally, the eighth dynamic exposure of the image with irregular morphology produces a relatively smooth graph without any prominent peaks, indicating the largely disordered state of the flow.

## V. SUMMARY AND CONCLUSIONS

We have acquired experimental data with temporal and spatial resolution sufficient to investigate the mixing transition induced by Richtmyer–Meshkov instability. The gas curtain data show quantitative features of the transition and provide a useful test problem for benchmarking codes designed to simulate highly perturbed flows.

The addition of fog droplets to the gas curtain increases the light scattering efficiency, resulting in images analogous to those produced with planar laser Rayleigh scattering, but with better dynamic range and temporal resolution. Thus up to 32 frames for each event can be acquired, intensity fields can be mapped to concentration fields, and the nonlinear growth, mode coupling, and mixing transition can be quantitatively investigated.

To study convergence and divergence effects on the small-scale structures, we add a long wavelength in the initial conditions to that of the primary perturbation used in previous studies. When the long-wavelength perturbation is convex with respect to the oncoming shock, the layer quickly flattens and mixing becomes readily apparent. For the situation where the long-wavelength perturbation is concave, convergence effects are noticed, and the growth of the smallest scales is suppressed.

The presence of two wavelengths of the same order in the initial conditions accelerates the onset of the mixing transition uniformly across the extent of the curtain.

Histogram analysis of the image intensity fields is successfully applied to our system which possesses diffuse initial conditions. By appropriately interpolating the data, a

two-peak histogram is produced with the peaks representing “unmixed” air and SF<sub>6</sub>, respectively. Early time straining along the curtain causes erosion of the peak associated with SF<sub>6</sub>. When the initial conditions possess perturbations from more than a single wavelength, a mixing transition can be identified by the rapid decay of this peak, corresponding to apparent mode coupling.

Application of the Mexican hat wavelet transform yields clear evidence of the growth of scales both smaller and larger than the initially imposed wavelength. Mushroom structures present due to the RM instability are readily quantified with the use of this wavelet. Plots of the rms-averaged values of the transform versus dilation show the growth of a broad spectrum of scales in the flow. Erosion of the peaks in the plots associated with spatially regular structures indicates the onset of mixing transition in good agreement with histogram analysis. These results clearly show the onset of a mixing transition in a shock-accelerated gas curtain with initial multimode perturbations.

## ACKNOWLEDGMENTS

We are grateful to Frank Kosel and Hadland Photonics, Ltd. for use of the SVR camera, to Lynn Veeseer, Doug Fulton, and Dave Oro for use of the Nd:YLF laser, and to Chris Gossein for technical assistance. We would also like to acknowledge Charles W. Cranfill, William J. Rider, James R. Kamm, Richard L. Holmes, and Timothy T. Clark for their helpful suggestions regarding this paper. Finally, special thanks to the referees for their insightful comments. This study was supported by the U.S. Department of Energy, Contract No. W-7405-ENG-36.

<sup>1</sup>J. D. Lindl, R. L. McCrory, and E. M. Campbell, “Progress toward ignition and burn propagation in inertial confinement fusion,” *Phys. Today* **45**, 32 (1992).

<sup>2</sup>W. D. Arnett, J. N. Bahcall, R. P. Kirshner, and S. E. Woosley, “Supernova 1987A,” *Annu. Rev. Astron. Astrophys.* **27**, 629 (1989).

<sup>3</sup>A. Burrows, J. Hayes, and B. A. Fryxell, “On the nature of core-collapse supernova explosions,” *Astrophys. J.* **450**, 830 (1995).

<sup>4</sup>E. E. Meshkov, “Instability of the interface of two gases accelerated by a shock wave,” *Izv. Akad. Nauk SSSR, Mekh. Zhidk. Gaza* **4**, 151 (1969), in Russian; *Izv. Acad. Sci., USSR, Fluid Dyn.* **4**, 101 (1969).

<sup>5</sup>R. F. Benjamin, “Shock and reshock of an unstable fluid interface,” *Proceedings of the First International Workshop on the Physics of Compressible Turbulent Mixing, Princeton, 24–27 Oct. 1998* (Lawrence Livermore National Laboratory Livermore, CA, 1991).

<sup>6</sup>R. F. Benjamin and J. N. Fritz, “Shock loading a rippled interface between liquids of different densities,” *Phys. Fluids* **30**, 331 (1987).

<sup>7</sup>M. Brouillette and B. Sturtevant, “Growth induced by multiple shock waves normally incident on plane gaseous interfaces,” *Physica D* **37**, 248 (1989).

<sup>8</sup>M. Brouillette and B. Sturtevant, “Experiments on the Richtmyer–Meshkov instability: Small-scale perturbations on a plane interface,” *Phys. Fluids A* **5**, 916 (1993).

<sup>9</sup>C. Cavailler, H. Croso, P. Gandeboeuf, J. F. Haas, and G. Rodriguez, “Results from the Vaujours vertical shock tube,” *Proceedings of the Third International Workshop on the Physics of Compressible Turbulent Mixing, Abbey of Royaumont, France, 17–19 June 1991* (Commissariat à l’Energie Atomique, France, 1991).

<sup>10</sup>R. Bonazza and B. Sturtevant, “X-ray measurements of growth rates at a gas interface accelerated by shock waves,” *Phys. Fluids* **8**, 2496 (1996).

<sup>11</sup>M. A. Jones and J. W. Jacobs, “A membraneless experiment for the study of Richtmyer–Meshkov instability of a shock-accelerated gas,” *Phys. Fluids* **9**, 3078 (1997).

- <sup>12</sup>J. W. Jacobs, D. L. Klein, D. G. Jenkins, and R. F. Benjamin, "Instability growth patterns of a shock-accelerated thin fluid layer," *Phys. Rev. Lett.* **70**, 583 (1993).
- <sup>13</sup>J. M. Budzinski, R. F. Benjamin, and J. W. Jacobs, "Influence of initial conditions on the flow patterns of a shock-accelerated thin fluid layer," *Phys. Fluids* **6**, 3510 (1994).
- <sup>14</sup>P. M. Rightley, P. Vorobieff, and R. F. Benjamin, "Evolution of a shock-accelerated thin fluid layer," *Phys. Fluids* **9**, 1770 (1997).
- <sup>15</sup>J. H. Konrad, "An experimental investigation of mixing in two-dimensional shear flows with applications to diffusion-limited chemical reactions," Ph.D. thesis, California Institute of Technology, 1977.
- <sup>16</sup>R. Breidenthal, "Chemically reacting, turbulent shear layer," *AIAA J.* **17**, 310 (1979).
- <sup>17</sup>L. P. Bernal and A. Roshko, "Streamwise vortex structure in plane mixing layers," *J. Fluid Mech.* **170**, 499 (1986).
- <sup>18</sup>J. C. Lasheras, J. S. Cho, and T. Maxworthy, "On the origin and evolution of streamwise vortical structures in a plane, free shear layer," *J. Fluid Mech.* **172**, 231 (1986).
- <sup>19</sup>J. F. Hawley and N. J. Zabusky, "Vortex paradigm for shock-accelerated density-stratified interfaces," *Phys. Rev. Lett.* **63**, 1241 (1989).
- <sup>20</sup>R. M. Baltrusaitis, M. L. Gittings, R. P. Weaver, R. F. Benjamin, and J. M. Budzinski, "Simulation of shock-generated instabilities," *Phys. Fluids* **8**, 2471 (1996).
- <sup>21</sup>C. W. Cranfill, "A new multifluid turbulent mix model," Los Alamos Report No. LA-UR-92-2484, available at NTIS, 1992.
- <sup>22</sup>M. Farge, "Wavelet transforms and their applications to turbulence," *Annu. Rev. Fluid Mech.* **24**, 395 (1992).
- <sup>23</sup>M. Farge, N. Kevlahan, V. Perrier, and E. Goirand, "Wavelets and turbulence," *Proc. IEEE* **84**, 639 (1996).
- <sup>24</sup>R. Everson, L. Sirovich, and K. Sreenivasan, "Wavelet analysis of the turbulent jet," *Phys. Lett. A* **145**, 314 (1990).
- <sup>25</sup>P. Vorobieff and D. Rockwell, "Wavelet filtering for topological decomposition of flow-fields," *Int. J. Imaging Syst. Technol.* **7**, 231 (1996).
- <sup>26</sup>R. Kraichnan, "On Kolmogorov's inertial range theories," *J. Fluid Mech.* **62**, 305 (1974).
- <sup>27</sup>L. Armi and P. Flament, "Cautionary remarks on the spectral interpretation of turbulent flows," *J. Geophys. Res.* **90**, 11779 (1985).
- <sup>28</sup>J. W. Jacobs, D. G. Jenkins, D. L. Klein, and R. F. Benjamin, "Nonlinear growth of the shock-accelerated instability of a thin fluid layer," *J. Fluid Mech.* **295**, 23 (1995).
- <sup>29</sup>P. Rightley and R. F. Benjamin, "High-speed flow visualization of fluid instabilities," *Proc. SPIE* **2869**, 327 (1996).
- <sup>30</sup>P. Vorobieff, P. Rightley, and R. Benjamin, "Growth rate and transition to turbulence of a gas curtain," to be published in *Proceedings of 6th IWPCTM Workshop, Marseille, 18-21 June 1997*.
- <sup>31</sup>F. R. Hama, "Streaklines in a perturbed shear flow," *Phys. Fluids* **5**, 644 (1962).
- <sup>32</sup>J. M. Ottino, "Mixing, chaotic advection, and turbulence," *Annu. Rev. Fluid Mech.* **22**, 207 (1990).
- <sup>33</sup>M. Lesieur, *Turbulence in Fluids* (Kluwer, Dordrecht, 1997).